


## Enhancement of the Spin-Mixing Conductance in Co-Fe-B/W Bilayers by Interface Engineering

Qi Lu, Yaojin Li, Bin Peng,<sup>\*</sup> Haowen Tang, Yao Zhang, Zhexi He, Liqian Wang, Chunlei Li, Wei Su, Qu Yang, Ziyao Zhou, and Ming Liu<sup>†</sup>

*Electronic Materials Research Laboratory, Key Laboratory of the Ministry of Education & International Center for Dielectric Research, School of Electronic and Information Engineering, Xi'an Jiaotong University, Xi'an 710049, China*

 (Received 14 May 2019; revised manuscript received 27 September 2019; published 13 December 2019)

In ferromagnetic/heavy-metal bilayer systems, spin-current transmission with high efficiency between the heavy-metal layer and the ferromagnetic layer across the interface is crucial for power-efficient spin-orbit torque magnetic random access memory (SOT MRAM). The spin-mixing conductance is one of the critical parameters that determines such efficiency at the interface. For the Co-Fe-B/W bilayer system, which is a promising candidate for SOT MRAM, improving the spin-current transmission efficiency at the interface by interface engineering, however, is not readily well studied. Here, we report that, by inserting an atomically thin  $\alpha$ -W layer at the interface of Co-Fe-B/W to construct the Co-Fe-B/ $\alpha$ -W/ $\beta$ -W trilayer system, the spin-mixing conductance can be enhanced by about 45%. A modified theoretical model is proposed that, in accordance with the experimental results, by considering the spin-backflow current as an equivalent spin resistance, the enhancement of spin-mixing conductance is attributed to suppression of the spin-backflow current by introducing  $\alpha$ -W. This study demonstrates that interfacial phase engineering between multiphases of the same heavy metal is effective at enhancing the spin-mixing conductance in ferromagnetic/heavy metal bilayer systems, which may further improve spin-current transmission efficiency and help realize power-efficient SOT MRAM based on Co-Fe-B/W systems.

DOI: [10.1103/PhysRevApplied.12.064035](https://doi.org/10.1103/PhysRevApplied.12.064035)

### I. INTRODUCTION

Manipulating magnetic moments by spin-orbit torque (SOT) is crucial for its profound physics and potential application in spintronic devices [1–3]. In a ferromagnet/heavy metal (FM/HM) bilayer, an in-plane charge current flowing through the HM layer will generate a pure spin current and, consequently, exert SOT in the adjacent FM layer, enabling power-efficient magnetization switching [4–6], fast domain wall motion [7–9], and magnetic nano-oscillation [10–12]. Although spin-orbit torques are much more effective than that of traditional spin-transfer torque for lowering the critical charge current density for magnetization switching, methods to further reduce the critical charge current density exerting SOT are attracting much attention in the field of spintronics [13–15]. Generally, the generation of the pure spin current in the HM layer and transmission of the spin current from the HM layer to the FM layer are two critical processes for exerting strong SOT. The former one is determined by the spin-orbit coupling of the HM materials, which is represented by spin Hall angle,  $\theta_{SH}$ , and the latter one is mainly determined

by the FM/HM interface, which is represented by the spin-mixing conductance,  $g_{\uparrow\downarrow}$  [16]. Hence, great efforts focus on exploring various heavy metals and other nonmagnetic (NM) materials with strong spin-orbit coupling that exhibit a large spin Hall angle [2,17–19]. On the other hand, if the interface limits the transmission efficiency of a spin current, the effective spin Hall angle in a given FM/HM bilayer system is much lower than that of the theoretical value, even for a HM layer with a large spin Hall angle [20]. Therefore, many efforts also focus on improving the spin-mixing conductance,  $g_{\uparrow\downarrow}$ , at the FM/HM interface to enhance the transmission efficiency of the spin current [21,22].

Spin-orbit torques are strongly dependent on the interface in FM/HM bilayer systems that are mainly determined by the spin-mixing conductance, and they can be modified by interface engineering and enhanced, in some cases. The interface engineering methods of FM/HM bilayer systems can be divided into two primary classes: inserting an atomically thin FM layer and inserting an atomically thin HM layer or NM layer. Early studies consider interface transparency, which is influenced by the spin-mixing conductance, as exemplified by the insertion of atomically thin magnetic layers at the Ni-Fe/Pt interface, which strongly modulates the magnitude of the spin-torque-derived spin

<sup>\*</sup>pengbin@xjtu.edu.cn

<sup>†</sup>mingliu@xjtu.edu.cn

Hall angle due to matching of the electronic properties in FM and HM layers [20]. Moreover, the spin-mixing conductance changes dramatically when the local microstructure of Co changes from fcc (111) to hcp (0001), which suggests differences in the effective specific interface spin resistance [23]. For inserting an atomically thin HM layer or NM layer, Cu is widely studied, but may reduce the spin-torque-derived spin Hall angle or spin pumping [20,24,25]. By building direct and interrupted interface conditions, inserting a 0.5 nm Cu layer in Ni-Fe/Pt systems reduces the dampinglike torque, fieldlike torque, and spin pumping by the same factor, depending on the spin-mixing conductance [24]. The voltage-driven  $O^{2-}$  migration near the FM/Pt interface enables tuning of the spin-orbit torques in a nonvolatile manner [26]. In addition, the interfacial charge density [27] and interfacial roughness [28] are also crucial roles for spin-mixing conductance. Thus, SOT devices with high efficiency and power consumption might be realized by carefully engineering the FM/HM interface [22].

The Co-Fe-B/W bilayer is one attractive system for next-generation spin-orbit torque magnetic random access memory (SOT MRAM) [29,30], not only because the Co-Fe-B layer is promising for magnetic tunnel junctions (MTJs) [31,32], but also  $\beta$ -phase tungsten ( $\beta$ -W) has the largest spin Hall angle among well-studied heavy metals of up to  $\theta_{SH} = 0.33$  [17]. They are also compatible with complementary metal-oxide-semiconductor (CMOS) technologies through magnetron sputtering [33], as compared with other newly found two-dimensional materials or topological insulators [13] with even larger spin Hall angles. To fully develop the application of Co-Fe-B/W systems in SOT devices, many studies have aimed to improve the SOT efficiency in Co-Fe-B/W structures. For the W layer, microstructure modification by oxygen incorporation [30] and band structure engineering via Ta alloying enhance the spin Hall angle of W greatly up to 0.5 [34]. The interfacial effects on SOT in Co-Fe-B/W structures is another significant method for achieving the goal [25]. So, improving the SOT efficiency in Co-Fe-B/W systems by interface engineering still requires further investigation.

Here, we systematically study the effect of engineering the interfacial layer on the spin-mixing conductance of a Co-Fe-B/ $\beta$ -W bilayer system and enhance the spin-mixing conductance about 45% by inserting an ultrathin (0.3 nm)  $\alpha$ -W layer. The theoretical model, which considers the spin-backflow factor as an equivalent spin resistance, is presented to describe our experiments and may have reference to other similar systems for interface engineering. Taking advantage of a large spin Hall angle from  $\beta$ -W for efficiently generating a pure spin current, and the advantage of high spin-mixing conductance at Co-Fe-B/ $\alpha$ -W/ $\beta$ -W for efficient spin-current transmission, our study demonstrates that interface engineering in the FM/HM bilayer system will improve the efficiency of SOT devices

by enhancing the spin-mixing conductance. Furthermore, this study lays the foundation for reducing the critical charge current density.

## II. EXPERIMENT

Co-Fe-B(6 nm)/inserting layer( $x$  nm)/W(6- $x$  nm) and Co-Fe-B(6 nm)/W(6 nm) multilayers with different phases of W are deposited onto a thermally oxidized Si substrate by dc magnetron sputtering at room temperature with a base pressure of less than  $1 \times 10^{-7}$  Torr. To grow  $\alpha$ -W, the deposition power is set to 30 W, with a deposition rate of about 0.02 nm/s, as monitored by a quartz crystal microbalance. To grow  $\beta$ -W, the deposition power is set to 7 W, with a deposition rate of 0.006 nm/s, since the low sputtering power is essential for the growth of  $\beta$ -W [35]. The Ar working pressure is 3 mTorr for depositing all layers.

The broadband ferromagnetic resonance (FMR) test is carried out with a FMR system using a microwave signal generator (N5173B, Keysight Technology) and a lock-in amplifier (SR830, Stanford Research). The sample is put onto a coplanar waveguide with the external magnetic field parallel to the thin-film surface. The sweeping magnetic field is modulated by a small 5 Oe alternating magnetic field. A vibrating sample magnetometer (7404, Lake Shore) is used to measure magnetic hysteresis loops. The structural characteristics of the samples are investigated by x-ray diffraction (D8 Advance, Bruker). The spin-pumping measurement is performed based on the refitting of an X-band (approximately equals 9.3 GHz) ESR system (JES-FA200, JOEL). The sample with dimensions of  $5 \times 10$  mm<sup>2</sup> is placed in the TE011 mode microwave cavity by a quartz rod. The magnetic field is applied parallel to the film and the microwave power is set at 10 mW. The voltage is measured by a nanovoltmeter (2182, Keithley). The distance between the electrodes is 7.5 mm. The resistivity is measured by a linear array four-point probe system with a test current of  $I = 1$  mA. All characterizations are performed at room temperature.

## III. RESULTS AND DISCUSSION

In the beginning, the phase structure of tungsten films is carefully controlled during fabrication. Figure 1(a) shows the x-ray diffraction (XRD) patterns of 20 nm tungsten films deposited at  $P = 7$  W and  $P = 30$  W on silicon substrates. The 20 nm W films deposited at  $P = 30$  W show both  $\alpha$ -W and  $\beta$ -W diffraction peaks, corresponding to the standard Joint Committee for Powder Diffraction Standards (JCPDS) No. 04-0806 and No. 47-1319, respectively. The ratio of  $\alpha$ -W/( $\alpha$ -W+ $\beta$ -W) is roughly estimated to be 84.6% from their relative intensities. The 20 nm W films deposited at  $P = 7$  W show predominately  $\beta$ -W diffraction peaks with only one low  $\alpha$ -W(110) diffraction peak, which is consistent with previous reports [36,37]. Therefore, a low deposition rate favors the formation of

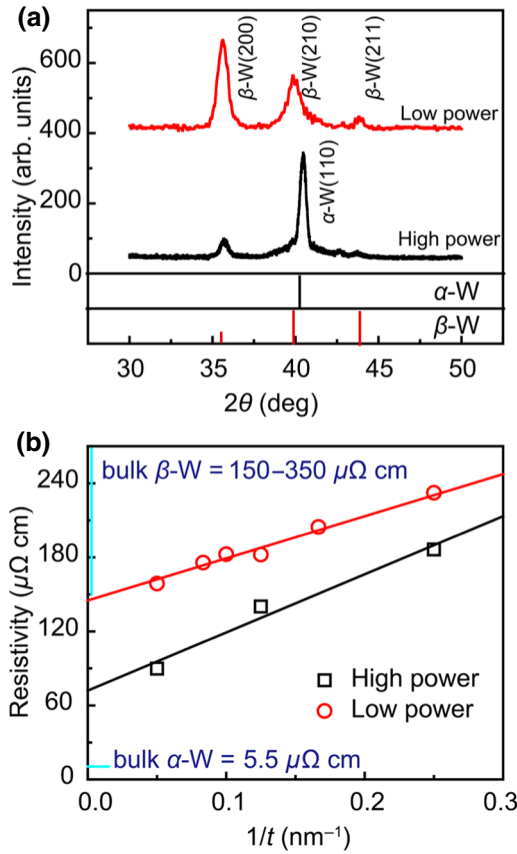


FIG. 1. (a) X-ray diffraction patterns of 20 nm tungsten films deposited at  $P = 7$  W and  $P = 30$  W on silicon substrates and (b) thickness-dependent resistivity of tungsten films.

$\beta$ -W, while a high deposition rate favors  $\alpha$ -W, since the low-power deposition ensures a low ultimate substrate temperature, which avoids the thermally activated phase transition from  $\beta$ -W to  $\alpha$ -W [38,39].

The phase structure of tungsten films studied here is further confirmed by measuring thickness-dependent resistivity, which is shown in Fig. 1(b). Recent work has shown a close relationship between the resistivity and spin Hall angle in heavy metals both experimentally and theoretically [40–42]. Thus,  $\beta$ -W with a large spin-orbit coupling should show high resistivity. A previous study has revealed that bulk  $\beta$ -W shows a much higher resistivity of around  $200 \mu\Omega \text{ cm}$  than that of  $\alpha$ -W, which is only about  $5.5 \mu\Omega \text{ cm}$  [43]. Here, the good quality of  $\beta$ -W films deposited at low power is confirmed [17]. The inverse thickness dependence of the resistivity is consistent with the classical surface scattering Fuchs-Sondheimer model [44]. The bulk resistivity of  $\beta$ -W obtained by linear extrapolation is determined and the result agrees well with a previous report in the range at  $150\text{--}350 \mu\Omega \text{ cm}$  [43]. Since a small fraction of  $\beta$ -W is also produced during growth of the  $\alpha$ -W thin film, the resistivity of  $\alpha$ -W obtained by linear extrapolation is

higher than that of the standard value for bulk  $\alpha$ -W  $5.5 \mu\Omega \text{ cm}$ , which mutually confirms with XRD result.

To investigate the effect of different interfacial conditions on spin-mixing conductance in Co-Fe-B/W systems, we perform broadband FMR measurements on Co-Fe-B/ $\beta$ -W with 0.5 nm Cu and the  $\alpha$ -W inserting layer. Figure 2(a) shows a schematic illustration of the broadband FMR measurement on a coplanar waveguide [45]. The FMR process pumps the spin current from Co-Fe-B to the adjacent W layer through the FM/HM interface. Figure 2(b) shows the typical FMR spectra for Co-Fe-B(6 nm) with different microwave frequencies by sweeping the magnetic field from zero to 1.2 kOe. The single line of FMR spectrum indicates that it is in a uniform precession mode. Figure 2(c) compares an expansion of FMR linewidth broadening at  $f = 9$  GHz for all samples. Compared with the Co-Fe-B single layer, the linewidths for Co-Fe-B/ $\alpha$ -W/ $\beta$ -W and Co-Fe-B/Cu/ $\beta$ -W increase around 38 Oe, which is a much larger value than those of 6.49 Oe for Co-Fe-B/ $\alpha$ -W and 22.58 Oe for Co-Fe-B/ $\beta$ -W; this may indicate the remarkable difference of spin dynamics in a ferromagnetic layer under different interfacial conditions [46].

The influence of the inserting layer on magnetization of the FM layer is ruled out. Here,  $4\pi M_s$  of the samples are obtained by fitting the microwave frequency,  $f$ , dependent resonance magnetic field,  $H_r$ , using the in-plane Kittel formula [47]:

$$\left(\frac{2\pi f}{\gamma}\right)^2 = (H_r + H_K + 4\pi M_s)(H_r + H_K). \quad (1)$$

The experimental value shows good agreement in fitting, and  $4\pi M_s$  of all samples remain relatively stable around 13 kOe [Fig. 3(a)]. The inserting layer has no significant impact on the intrinsic magnetic property of the FM layer, and thus, indicates that the linewidth broadening originates from the interface. The in-plane VSM test is performed for all samples and is illustrated in Fig. 3(c). All samples show consistent saturation magnetization of about  $1200 \text{ emu/cm}^3$ , which corresponds well to the previous study [48] and our FMR test. Thus, the influence of the inserting layer on the intrinsic magnetic property can be excluded.

Figure 3(b) shows the linear fitting of FMR linewidth  $\Delta H$  with respect to the microwave frequency  $f$ . It clearly shows that the FMR linewidth varies linearly with the microwave frequency. The Gilbert damping constant,  $\alpha$ , which is proportional to the slope of the  $\Delta H$ - $f$  plot can be derived from [46]

$$\Delta H = \Delta H_0 + \frac{4\pi\alpha f}{|\gamma|}, \quad (2)$$

where  $\gamma$  is the gyromagnetic ratio and  $\Delta H_0$  represents the inhomogeneous linewidth of the magnetic layer. The

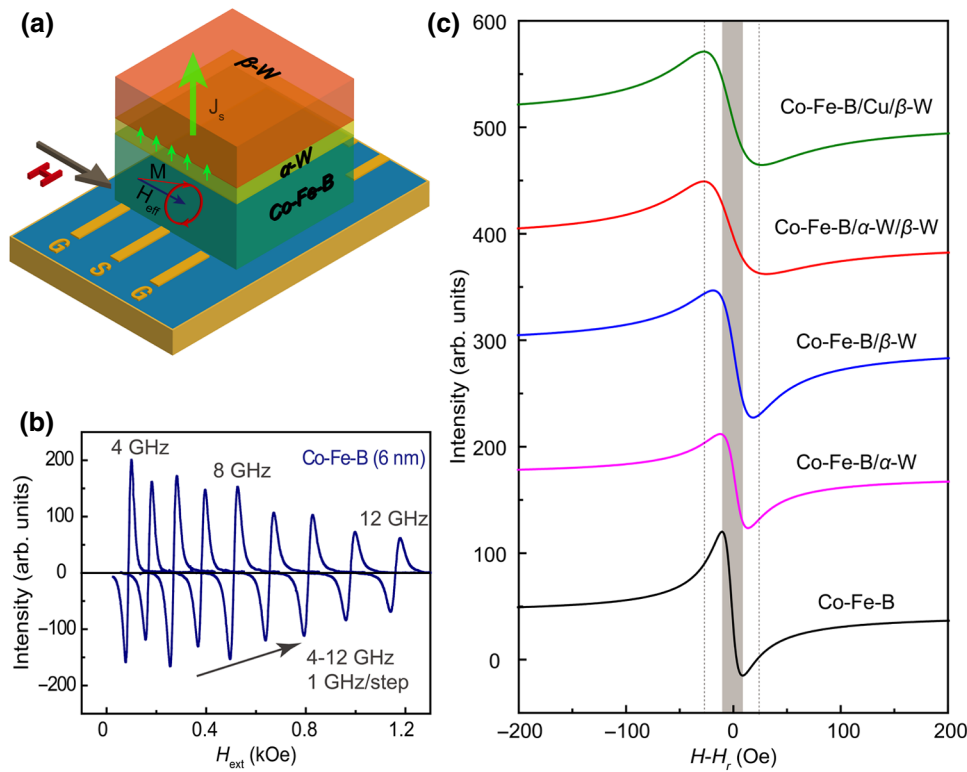


FIG. 2. (a) Schematic of broadband FMR measurement and spin-current transmission across the FM/HM interface. (b) FMR spectra recorded in sweeping-field mode with different microwave frequencies for Co-Fe-B(6 nm). (c) FMR spectra at 9 GHz for different samples.

single Co-Fe-B layer shows a low Gilbert damping constant,  $\alpha = 0.0027$ , which is consistent with the previous study [49]. When the Co-Fe-B layer is covered with  $\beta$ -W(6 nm) and  $\alpha$ -W(6 nm), the Gilbert damping increases to 0.0066 and 0.0044, respectively. The enhancement of

Gilbert damping due to angular momentum loss in the FM layer represents the spin-injection process to the HM layer. The local interfacial structure has a significant impact on the Gilbert damping constant. Thus, it can be modulated by inserting a new atomically thin layer into the

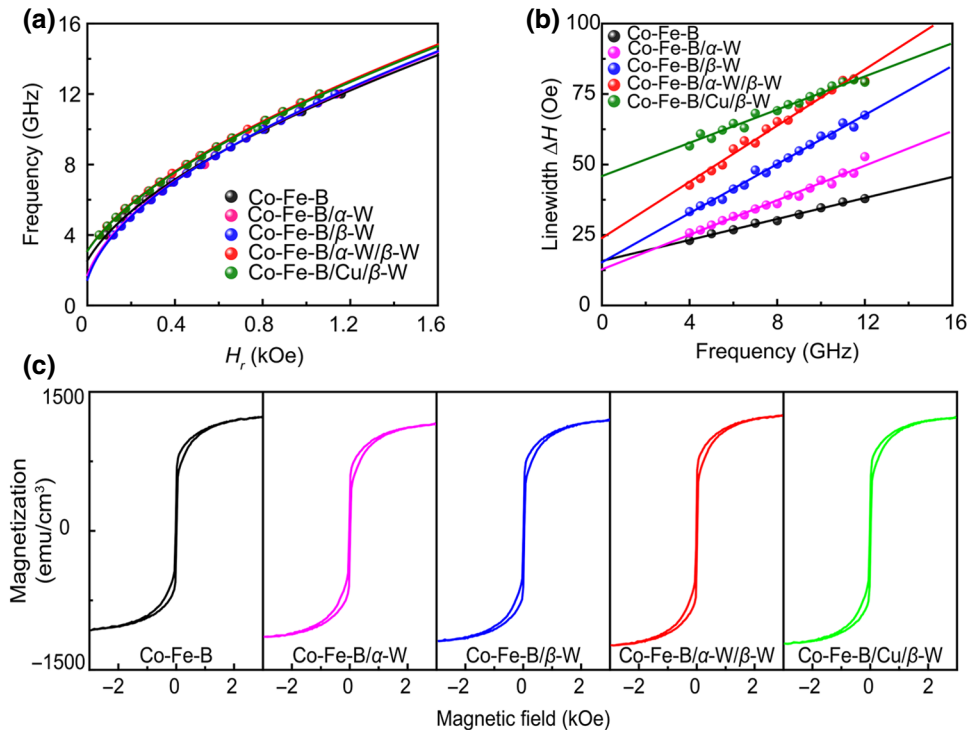


FIG. 3. (a) FMR resonance field,  $H_r$ , as a function of the microwave frequency. (b) Peak-to-peak FMR linewidth versus microwave frequency. (c) In-plane magnetic hysteresis loops of Co-Fe-B/W systems.

Co-Fe-B/ $\beta$ -W system. For the case of inserting 0.5 nm Cu, the Gilbert damping constant dramatically decreases to 0.0043, while inserting 0.5 nm  $\alpha$ -W results in a maximum Gilbert damping constant of 0.0076 in all samples. Here, the inhomogeneous linewidth  $\Delta H_0$  results from the inhomogeneity of the magnetic films and depends on the lattice mismatch at the FM/HM interface [23]. The 0.5 nm inserting layer will induce greater lattice mismatch between the FM layer and HM layer. Hence, samples with a 0.5 nm ultrathin inserting layer show a higher inhomogeneous linewidth,  $\Delta H_0$ , in Fig. 3(b), while the pure Co-Fe-B layer and bilayer samples show a lower  $\Delta H_0$ . Since linear fitting enables separation of the Gilbert damping constant from the total FMR linewidth, the inhomogeneous linewidth will not affect the calculation results of Gilbert damping constant.

The spin current transferring from the FM layer into adjacent the NM layer will slow down the precession of magnetization corresponding to an enhancement of the Gilbert damping constant. Hence, the Gilbert damping constant,  $\alpha$ , and  $4\pi M_s$  provide a method to calculate the spin-mixing conductance,  $g_{\uparrow\downarrow}$ , by [50]

$$g_{\uparrow\downarrow} = \frac{4\pi M_s t_{\text{FM}}}{\gamma \hbar} (\alpha_{\text{comb}} - \alpha), \quad (3)$$

where  $t_{\text{FM}}$  is the thickness of the ferromagnetic layer,  $\gamma$  is the gyromagnetic ratio,  $\alpha$  represents the Gilbert damping constant for a single magnetic layer, and  $\alpha_{\text{comb}}$  is the Gilbert damping constant for the whole FM/NM structure. The interface spin-mixing conductance is proportional to the enhancement of the Gilbert damping constant,  $\alpha_{\text{comb}} - \alpha$ . The calculation results for all samples are summarized in Table I within in the Supplemental Material [51]. When 0.5 nm  $\alpha$ -W inserts at the Co-Fe-B/ $\beta$ -W interface, the spin-mixing conductance is improved by nearly 30%, while the 0.5 nm Cu inserting layer reduces the spin-mixing conductance by around 58%, which is consistent with previous studies, and thus, proves that the spin-mixing conductance can be enhanced by optimizing the interfacial condition through inserting a well-chosen material.

To further obtain a deeper understanding of the effect on the  $\alpha$ -W inserting layer and find the best thickness for optimizing the spin-mixing conductance, Fig. 4 shows the inserting-layer-thickness dependence on the spin-mixing conductance in Co-Fe-B(6 nm)/ $\alpha$ -W( $x$  nm)/ $\beta$ -W(6- $x$  nm). The evolution of the spin-mixing conductance can be divided into two regions. When the inserting layer is atomically thin in region I, the spin-mixing conductance increases and reaches a maximum value of about  $18.03 \times 10^{17} \text{ m}^{-2}$  at 0.3 nm thickness. In region II, the spin-mixing conductance shows an inversely proportional tendency to the thickness of the inserting layer. It agrees with the theory of spin-mixing conductance in trilayer

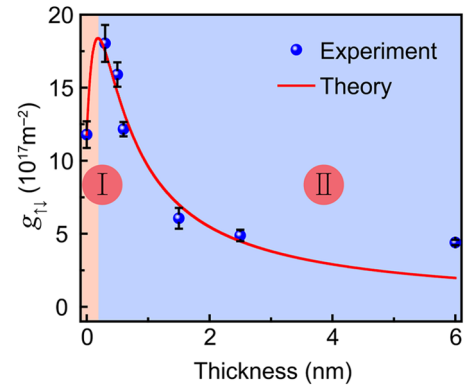


FIG. 4. Spin-mixing conductance versus thickness of the inserting layer for Co-Fe-B(6 nm)/ $\alpha$ -W( $x$  nm)/ $\beta$ -W(6- $x$  nm). The red line represents the theoretical result.

systems [52,53] and converges on a reasonable value of spin-mixing conductance for sample Co-Fe-B(6 nm)/ $\alpha$ -W(6 nm) at around  $5.44 \times 10^{17} \text{ m}^{-2}$ .

The spin accumulation will induce a spin-current backflow,  $I_s^{\text{back}}$ , which weakens the total spin current,  $I_s^{\text{net}} = I_s^{\text{pump}} - I_s^{\text{back}}$ . By considering a spin-backflow factor,  $\beta$ , the spin-current transmission theory for FM/NM/spin sink trilayer systems is proposed [54,55]. The spin-backflow factor,  $\beta$ , which is related to the spin-mixing conductance, can be expressed as

$$g_{\uparrow\downarrow}(\beta) = \frac{g_0}{1 + \beta g_0}, \quad (4)$$

where  $g_0$  is the intrinsic spin-mixing conductance for Co-Fe-B/ $\beta$ -W without the spin-backflow current. Neglecting spin scattering at the NM/spin sink layer interface, the spin-backflow factor  $\beta$  for a trilayer system is given by [54]

$$\beta = \frac{1}{2\pi g_s} \frac{g_s \cosh(d/\lambda) + g_s^S \sinh(d/\lambda) \tanh(d^S/\lambda^S)}{g_s \sinh(d/\lambda) + g_s^S \cosh(d/\lambda) \tanh(d^S/\lambda^S)}, \quad (5)$$

where  $d$  and  $\lambda$  are the thickness and spin-diffusion length of the NM layer, respectively;  $g_s$  is the spin conductivity per unit area related to the charge conductivity,  $\sigma$ , given by  $g_s = (\hbar\sigma)/(2e^2\lambda)$ . Superscript  $S$  represents the parameters for the spin-sink layer. Here, the inserting  $\alpha$ -W layer will reduce the spin-backflow factor for the whole structure, while inserting the Cu layer increases the factor as shown in the Supplemental Material [51]. These results indicate that the enhancement of spin-mixing conductance originates from a reduction of the spin-backflow factor. Figure 5 illustrates the mechanism of interface engineering to enhance the spin-mixing conductance through suppression of the spin-backflow current.

In addition, the spin-mixing conductance for a trilayer system FM/NM1/NM2 is related to the inverse spin conductance of the inserting layer in series, with its two

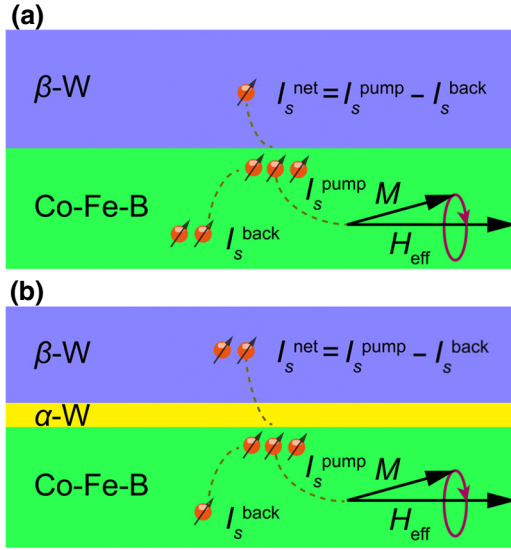


FIG. 5. Mechanism of spin-current transmission in Co-Fe-B/ $\beta$ -W modulated by an inserting layer.

interfaces in the limit of vanishing spin-flip processes in the inserting layer [52,54]. Here, we consider introducing the spin-backflow factor at the NM2/space interface into previous work. In the limiting case that the spin resistance of NM1/NM2 interface is very small and can be neglected, we have

$$g_{\uparrow\downarrow\text{trilayer}} = \frac{1}{(1/g_0) + \beta + (2e^2/h\rho t c)}, \quad (6)$$

where  $\beta$  is the spin-backflow factor in Eq. (5), which is added as an equivalent spin resistance to describe the influence of spin-backflow current at the  $\beta$ -W/space interface on the total spin-mixing conductance. Correction factor  $c$  is used to describe the imperfect interface due to the small amount of  $\beta$ -W in the  $\alpha$ -W inserting layer, as discussed in the XRD analysis above.  $\rho$  and  $t$  represent the resistivity and thickness of the inserting layer, respectively.

The following standard values of the parameters are taken from previous studies [43,56,57]:  $\lambda_{\alpha\text{-W}} = 3.8$  nm,  $\lambda_{\beta\text{-W}} = 2.5$  nm,  $\sigma_{\alpha\text{-W}} = 5.5 \mu\Omega$  cm, and  $\sigma_{\beta\text{-W}} = 350 \mu\Omega$  cm;  $g_0$  is acquired by fitting the spin-mixing conductance of Co-Fe-B(6)/ $\beta$ -W(6) into Eq. (4). The red curve in Fig. 4 shows the theoretical result using the standard values above with a correction factor,  $c$ , equal to 195.1. The theoretical analysis agrees well with the experimental data and provides a relatively reasonable extrapolated result for the pure  $\alpha$ -W condition. Such results support our observation that the spin-mixing conductance increases at first and then declines due to the combined effects of the spin-backflow factor and series model of spin resistance, in which the spin-backflow factor dominates region I and the series model of spin resistance dominates region II.

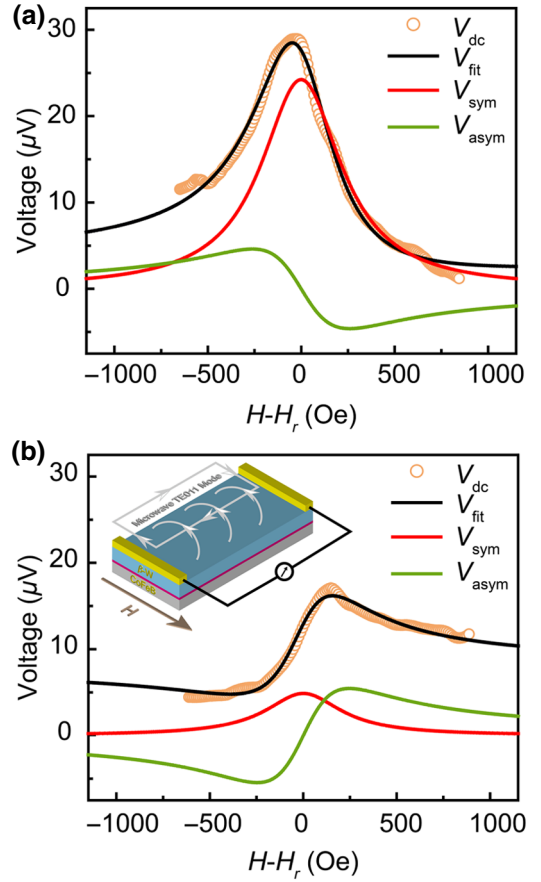


FIG. 6. Spin-pumping voltage signals for (a) Co-Fe-B(6 nm)/ $\alpha$ -W(0.3 nm)/ $\beta$ -W(5.7 nm) and (b) Co-Fe-B(6 nm)/ $\beta$ -W(6 nm) systems. Inset in (b) is a schematic of the spin-pumping measurement setup in a microwave cavity.

To directly determine the spin-current transmission process at the FM/HM interface and compare the value of net spin current with different interface conditions, we conduct spin-pumping measurements in a microwave cavity, as shown in Fig. 6. To obtain the contribution of the inverse spin Hall effect and other galvanomagnetic effects, such as anisotropic magnetoresistance effect, and anomalous Hall effect from the total dc voltage, we analyze the Lorentzian symmetric part and Lorentzian antisymmetric part derived from the best fitting of [58]

$$V_{\text{dc}} = A_s \frac{\Delta H^2}{[(H - H_r)^2 + \Delta H^2]} + L_a \frac{(H - H_r) \Delta H}{[(H - H_r)^2 + \Delta H^2]} + \text{offset}. \quad (7)$$

Figure 6 shows the measured dc voltage with each fitting component. The antisymmetric part of voltage due to galvanomagnetic effects is the same for the two samples, which indicates the same galvanomagnetic property in the Co-Fe-B layer [59,60]. The large spin-pumping signals of about  $23 \mu\text{V}$  generated by the inverse spin Hall effect

in Fig. 6(a) directly prove a high spin current in Co-Fe-B(6 nm)/ $\alpha$ -W(0.3 nm)/ $\beta$ -W(5.7 nm) due to the enhancement of spin-mixing conductance, and the overall effect is beneficial to achieve efficient spin-current transmission. The combination of broadband FMR and spin-pumping measurements can be a reliable approach to determine the spin-current transmission process [24,61,62]. Thus, we obtain a modified system with both high spin-mixing conductance and strong spin Hall effect to enable efficient spin-current transmission.

#### IV. CONCLUSION

We investigate the spin-mixing conductance under different interfacial conditions in the Co-Fe-B/ $\beta$ -W system. By comparing different inserting-layer conditions, we find that Co-Fe-B(6 nm)/ $\alpha$ -W(0.3 nm)/ $\beta$ -W(5.7 nm) shows about 45% enhancement of spin-mixing conductance relative to that of the Co-Fe-B(6 nm)/ $\beta$ -W(6 nm) system. A modified theoretical model is also developed by introducing the spin-backflow factor as an equivalent spin resistance, which is suppressed by introducing ultrathin  $\alpha$ -W that results in the enhancement of spin-mixing conductance. Through such interfacial phase engineering, the spin-mixing conductance is enhanced and a strong spin Hall effect is still maintained at the heavy-metal layer; this will pave the way for highly efficient low-power-consumption SOT-based spintronic devices through the design of Co-Fe-B/ $\beta$ -W systems.

#### ACKNOWLEDGMENTS

The work is supported by the National Key R&D Program of China (Grant No. 2018YFB0407601), the Natural Science Foundation of China (Grants No. 51902248, No. 11534015, and No. 51602244), the China Postdoctoral Science Foundation (Grant No. 2019M663693), the National 111 Project of China (Grant No. B14040), and the Fundamental Research Funds for the Central Universities (Grant No. xjj2018207). We thank Dr. Chang Huang at Instrument Analysis Center of Xi'an Jiaotong University for his assistance on XRD measurements and analysis.

---

[1] A. Brataas, A. D. Kent, and H. Ohno, Current-induced torques in magnetic materials, *Nat. Mater.* **11**, 372 (2012).  
 [2] L. Q. Liu, C. F. Pai, Y. Li, H. W. Tseng, D. C. Ralph, and R. A. Buhrman, Spin-torque switching with the giant spin hall effect of tantalum, *Science* **336**, 555 (2012).  
 [3] Y. Fan, P. Upadhyaya, X. Kou, M. Lang, S. Takei, Z. Wang, J. Tang, L. He, L. T. Chang, M. Montazeri, G. Yu, W. Jiang, T. Nie, R. N. Schwartz, Y. Tserkovnyak, and K. L. Wang, Magnetization switching through giant spin-orbit torque in a magnetically doped topological insulator heterostructure, *Nat. Mater.* **13**, 699 (2014).

[4] Y. C. Lau, D. Betto, K. Rode, J. M. Coey, and P. Stamenov, Spin-orbit torque switching without an external field using interlayer exchange coupling, *Nat. Nanotechnol.* **11**, 758 (2016).  
 [5] I. M. Miron, K. Garello, G. Gaudin, P. J. Zermatten, M. V. Costache, S. Auffret, S. Bandiera, B. Rodmacq, A. Schuhl, and P. Gambardella, Perpendicular switching of a single ferromagnetic layer induced by in-plane current injection, *Nature* **476**, 189 (2011).  
 [6] M. X. Wang, W. L. Cai, D. Q. Zhu, Z. H. Wang, J. Kan, Z. Y. Zhao, K. H. Cao, Z. L. Wang, Y. G. Zhang, T. R. Zhang, C. Park, J. P. Wang, A. Fert, and W. S. Zhao, Field-free switching of a perpendicular magnetic tunnel junction through the interplay of spin-orbit and spin-transfer torques, *Nat. Electron.* **1**, 582 (2018).  
 [7] P. P. J. Haazen, E. Mure, J. H. Franken, R. Lavrijsen, H. J. M. Swagten, and B. Koopmans, Domain wall depinning governed by the spin Hall effect, *Nat. Mater.* **12**, 299 (2013).  
 [8] K. S. Ryu, S. H. Yang, L. Thomas, and S. S. P. Parkin, Chiral spin torque arising from proximity-induced magnetization, *Nat. Commun.* **5**, 4910 (2014).  
 [9] B. Zhang, Y. Xu, W. Zhao, D. Zhu, X. Lin, M. Hehn, G. Malinowski, D. Ravelosona, and S. Mangin, Energy-Efficient Domain-Wall Motion Governed by the Interplay of Helicity-Dependent Optical Effect and Spin-Orbit Torque, *Phys. Rev. Appl.* **11**, 034001 (2019).  
 [10] V. E. Demidov, S. Urazhdin, H. Ulrichs, V. Tiberkevich, A. Slavin, D. Baither, G. Schmitz, and S. O. Demokritov, Magnetic nano-oscillator driven by pure spin current, *Nat. Mater.* **11**, 1028 (2012).  
 [11] L. Q. Liu, C. F. Pai, D. C. Ralph, and R. A. Buhrman, Magnetic Oscillations Driven by the Spin Hall Effect in 3-Terminal Magnetic Tunnel Junction Devices, *Phys. Rev. Lett.* **109**, 186602 (2012).  
 [12] Z. Duan, A. Smith, L. Yang, B. Youngblood, J. Lindner, V. E. Demidov, S. O. Demokritov, and I. N. Krivorotov, Nanowire spin torque oscillator driven by spin orbit torques, *Nat. Commun.* **5**, 6616 (2014).  
 [13] M. Dc, R. Grassi, J. Y. Chen, M. Jamali, D. Reifsnnyder Hickey, D. Zhang, Z. Zhao, H. Li, P. Quarterman, Y. Lv, M. Li, A. Manchon, K. A. Mkhoyan, T. Low, and J. P. Wang, Room-temperature high spin-orbit torque due to quantum confinement in sputtered BixSe(1-x) films, *Nat. Mater.* **17**, 800 (2018).  
 [14] C. O. Avci, A. Quindeau, C. F. Pai, M. Mann, L. Caretta, A. S. Tang, M. C. Onbasli, C. A. Ross, and G. S. Beach, Current-induced switching in a magnetic insulator, *Nat. Mater.* **16**, 309 (2017).  
 [15] Z. Wang, L. Zhang, M. Wang, Z. Wang, D. Zhu, Y. Zhang, and W. Zhao, High-Density NAND-like spin transfer torque memory With spin orbit torque erase operation, *IEEE Electron Device Lett.* **39**, 343 (2018).  
 [16] M. Zwierzycki, Y. Tserkovnyak, P. J. Kelly, A. Brataas, and G. E. W. Bauer, First-principles study of magnetization relaxation enhancement and spin transfer in thin magnetic films, *Phys. Rev. B* **71**, 064420 (2005).  
 [17] C. F. Pai, L. Q. Liu, Y. Li, H. W. Tseng, D. C. Ralph, and R. A. Buhrman, Spin transfer torque devices utilizing the giant spin Hall effect of tungsten, *Appl. Phys. Lett.* **101**, 122404 (2012).

- [18] T. Kimura, Y. Otani, T. Sato, S. Takahashi, and S. Maekawa, Room-Temperature Reversible Spin Hall Effect, *Phys. Rev. Lett.* **98**, 156601 (2007).
- [19] L. Zhu, L. Zhu, S. Shi, M. Sui, D. C. Ralph, and R. A. Buhrman, Enhancing Spin-Orbit Torque by Strong Interfacial Scattering From Ultrathin Insertion Layers, *Phys. Rev. Appl.* **11**, 061004 (2019).
- [20] W. Zhang, W. Han, X. Jiang, S. H. Yang, and S. S. P. Parkin, Role of transparency of platinum–ferromagnet interfaces in determining the intrinsic magnitude of the spin hall effect, *Nat. Phys.* **11**, 496 (2015).
- [21] X. Qiu, W. Legrand, P. He, Y. Wu, J. Yu, R. Ramaswamy, A. Manchon, and H. Yang, Enhanced Spin-Orbit Torque via Modulation of Spin Current Absorption, *Phys. Rev. Lett.* **117**, 217206 (2016).
- [22] C.-F. Pai, Y. Ou, L. H. Vilela-Leão, D. C. Ralph, and R. A. Buhrman, Dependence of the efficiency of spin hall torque on the transparency of Pt/ferromagnetic layer interfaces, *Phys. Rev. B* **92**, 064426 (2015).
- [23] M. Tokac, S. A. Bunyayev, G. N. Kakazei, D. S. Schmool, D. Atkinson, and A. T. Hindmarch, Interfacial Structure Dependent Spin Mixing Conductance in Cobalt Thin Films, *Phys. Rev. Lett.* **115**, 056601 (2015).
- [24] T. Nan, S. Emori, C. T. Boone, X. Wang, T. M. Oxholm, J. G. Jones, B. M. Howe, G. J. Brown, and N. X. Sun, Comparison of spin-orbit torques and spin pumping across NiFe/Pt and NiFe/Cu/Pt interfaces, *Phys. Rev. B* **91**, 214416 (2015).
- [25] J. Zhang, T. Phung, B. P. Hughes, S. H. Yang, C. Garg, Y. Jiang, and S. S. P. Parkin, Effect of interfacial insertion layers on the spin–orbit torque in W(O)|CoFeB heterostructures, *Appl. Phys. Express* **12**, 033001 (2019).
- [26] H. Y. An, T. Ohno, Y. Kanno, Y. Kageyama, Y. Monnai, H. Maki, J. Shi, and K. Ando, Current-induced magnetization switching using an electrically insulating spin-torque generator, *Sci. Adv.* **4**, 2250 (2018).
- [27] L. Wang, Z. Lu, J. Xue, P. Shi, Y. Tian, Y. Chen, S. Yan, L. Bai, and M. Harder, Electrical Control of Spin-Mixing Conductance in a Y3Fe5O12/Platinum Bilayer, *Phys. Rev. Appl.* **11**, 044060 (2019).
- [28] Q. Zhang, S. Hikino, and S. Yunoki, First-principles study of the spin-mixing conductance in Pt/Ni81Fe19 junctions, *Appl. Phys. Lett.* **99**, 172105 (2011).
- [29] C. He, G. Yu, C. Grezes, J. Feng, Z. Zhao, S. A. Razavi, Q. Shao, A. Navabi, X. Li, Q. L. He, M. Li, J. Zhang, K. L. Wong, D. Wei, G. Zhang, X. Han, P. K. Amiri, and K. L. Wang, Spin-Torque Ferromagnetic Resonance in W/CoFeB/W/CoFeB/MgO Stacks, *Phys. Rev. Appl.* **10**, 034067 (2018).
- [30] K. U. Demasius, T. Phung, W. Zhang, B. P. Hughes, S. H. Yang, A. Kellock, W. Han, A. Pushp, and S. S. Parkin, Enhanced spin-orbit torques by oxygen incorporation in tungsten films, *Nat. Commun.* **7**, 10644 (2016).
- [31] S. Ikeda, K. Miura, H. Yamamoto, K. Mizunuma, H. D. Gan, M. Endo, S. Kanai, J. Hayakawa, F. Matsukura, and H. Ohno, A perpendicular-anisotropy CoFeB-MgO magnetic tunnel junction, *Nat. Mater.* **9**, 721 (2010).
- [32] D. C. Worledge, G. Hu, D. W. Abraham, J. Z. Sun, P. L. Trouilloud, J. Nowak, S. Brown, M. C. Gaidis, E. J. O’Sullivan, and R. P. Robertazzi, Spin torque switching of perpendicular Ta|CoFeB|MgO-based magnetic tunnel junctions, *Appl. Phys. Lett.* **98**, 022501 (2011).
- [33] H. Sato, E. C. I. Enobio, M. Yamanouchi, S. Ikeda, S. Fukami, S. Kanai, F. Matsukura, and H. Ohno, Properties of magnetic tunnel junctions with a MgO/CoFeB/Ta/CoFeB/MgO recording structure down to junction diameter of 11 nm, *Appl. Phys. Lett.* **105**, 062403 (2014).
- [34] X. Sui, C. Wang, J. Kim, J. Wang, S. H. Rhim, W. Duan, and N. Kioussis, Giant enhancement of the intrinsic spin Hall conductivity in  $\beta$ -tungsten via substitutional doping, *Phys. Rev. B* **96**, 241105 (2017).
- [35] Q. Hao, W. Z. Chen, and G. Xiao, Beta ( $\beta$ ) tungsten thin films: Structure, electron transport, and giant spin Hall effect, *Appl. Phys. Lett.* **106**, 182403 (2015).
- [36] L. Neumann, D. Meier, J. Schmalhorst, K. Rott, G. Reiss, and M. Meinert, Temperature dependence of the spin Hall angle and switching current in the nc-W(O)/CoFeB/MgO system with perpendicular magnetic anisotropy, *Appl. Phys. Lett.* **109**, 142405 (2016).
- [37] W. Skowroński, M. Cecot, J. Kanak, S. Ziętek, T. Stobiecki, L. Yao, S. van Dijken, T. Nozaki, K. Yakushiji, and S. Yuasa, Temperature dependence of spin-orbit torques in W/CoFeB bilayers, *Appl. Phys. Lett.* **109**, 062407 (2016).
- [38] P. Collot, B. Agius, P. Estrache, M. C. Hugon, M. Froment, J. Bessot, and Y. Crassin, Physicochemical properties in tungsten films deposited by radio-frequency magnetron sputtering, *J. Vac. Sci. Technol. A* **6**, 2319 (1988).
- [39] A. J. Narasimham, M. Medikonda, A. Matsubayashi, P. Khare, H. Chong, R. J. Matyi, A. Diebold, and V. P. LaBella, Fabrication of 5–20 nm thick  $\beta$ -W films, *AIP Adv.* **4**, 117139 (2014).
- [40] J. W. Lee, Y.-W. Oh, S.-Y. Park, A. I. Figueroa, G. van der Laan, G. Go, K.-J. Lee, and B.-G. Park, Enhanced spin-orbit torque by engineering Pt resistivity in Pt/Co/AlOx structures, *Phys. Rev. B* **96**, 064405 (2017).
- [41] L. Wang, R. J. H. Wesselink, Y. Liu, Z. Yuan, K. Xia, and P. J. Kelly, Giant Room Temperature Interface Spin Hall and Inverse Spin Hall Effects, *Phys. Rev. Lett.* **116**, 196602 (2016).
- [42] E. Sagasta, Y. Omori, M. Isasa, M. Gradhand, L. E. Hueso, Y. Niimi, Y. Otani, and F. Casanova, Tuning the spin Hall effect of Pt from the moderately dirty to the superclean regime, *Phys. Rev. B* **94**, 060412 (2016).
- [43] D. Choi, B. Wang, S. Chung, X. Liu, A. Darbal, A. Wise, N. T. Nuhfer, K. Barmak, A. P. Warren, K. R. Coffey, and M. F. Toney, Phase, grain structure, stress, and resistivity of sputter-deposited tungsten films, *J. Vac. Sci. Technol. A* **29**, 051512 (2011).
- [44] E. H. Sondheimer, The mean free path of electrons in metals, *Adv. Phys.* **50**, 499 (2001).
- [45] S. S. Kalarickal, P. Krivosik, M. Z. Wu, C. E. Patton, M. L. Schneider, P. Kabos, T. J. Silva, and J. P. Nibarger, Ferromagnetic resonance linewidth in metallic thin films: Comparison of measurement methods, *J. Appl. Phys.* **99**, 093909 (2006).
- [46] K. Zakeri, J. Lindner, I. Barsukov, R. Meckenstock, M. Farle, U. von Horsten, H. Wende, W. Keune, J. Rocker, S. S. Kalarickal, K. Lenz, W. Kuch, K. Baberschke, and



- Z. Frait, Spin dynamics in ferromagnets: Gilbert damping and two-magnon scattering, *Phys. Rev. B* **76**, 104416 (2007).
- [47] C. Kittel, On the theory of ferromagnetic resonance absorption, *Phys. Rev.* **73**, 155 (1948).
- [48] M. Belmeguenai, K. Aitoukaci, F. Zighem, M. S. Gabor, T. Petrison, R. B. Mos, and C. Tiusan, Investigation of the annealing temperature dependence of the spin pumping in Co<sub>20</sub>Fe<sub>60</sub>B<sub>20</sub>/Pt systems, *J. Appl. Phys.* **123**, 113905 (2018).
- [49] A. Conca, J. Greser, T. Sebastian, S. Klingler, B. Obry, B. Leven, and B. Hillebrands, Low spin-wave damping in amorphous Co<sub>40</sub>Fe<sub>40</sub>B<sub>20</sub> thin films, *J. Appl. Phys.* **113**, 213909 (2013).
- [50] O. Mosendz, J. E. Pearson, F. Y. Fradin, G. E. Bauer, S. D. Bader, and A. Hoffmann, Quantifying Spin Hall Angles From Spin Pumping: Experiments and Theory, *Phys. Rev. Lett.* **104**, 046601 (2010).
- [51] See the Supplemental Material at <http://link.aps.org/supplemental/10.1103/PhysRevApplied.12.064035> for more detailed information about the parameters derived from the FMR spectra, XRD analysis of W films with different deposition power, the role of the spin backflow factor on spin-mixing conductance, and the calculation results of spin-mixing conductance with ideal interface.
- [52] Y. Tserkovnyak, A. Brataas, and G. E. W. Bauer, Spin pumping and magnetization dynamics in metallic multilayers, *Phys. Rev. B* **66**, 224403 (2002).
- [53] C. H. Du, H. L. Wang, F. Y. Yang, and P. C. Hammel, Enhancement of Pure Spin Currents in Spin Pumping Y<sub>3</sub>Fe<sub>5</sub>O<sub>12</sub>/Cu/Metal Trilayers Through Spin Conductance Matching, *Phys. Rev. Appl.* **1**, 044004 (2014).
- [54] K. Harii, Z. Qiu, T. Iwashita, Y. Kajiwara, K. Uchida, K. Ando, T. An, Y. Fujikawa, and E. Saitoh, Spin pumping in a ferromagnetic/nonmagnetic/spin-sink trilayer film: Spin current termination, *Key Eng. Mater.* **508**, 266 (2012).
- [55] K. Roy, Spin-Circuit Representation of Spin Pumping, *Phys. Rev. Appl.* **8**, 011001 (2017).
- [56] D. Jhahhria, N. Behera, D. K. Pandya, and S. Chaudhary, Dependence of spin pumping in W/CoFeB heterostructures on the structural phase of tungsten, *Phys. Rev. B* **99**, 014430 (2019).
- [57] W. Park, D. V. Baxter, S. Steenwyk, I. Moraru, W. P. Pratt, and J. Bass, Measurement of resistance and spin-memory loss (spin relaxation) at interfaces using sputtered current perpendicular-to-plane exchange-biased spin valves, *Phys. Rev. B* **62**, 1178 (2000).
- [58] M. Wahler, N. Homonnay, T. Richter, A. Muller, C. Eisen-schmidt, B. Fuhrmann, and G. Schmidt, Inverse spin Hall effect in a complex ferromagnetic oxide heterostructure, *Sci. Rep.* **6**, 28727 (2016).
- [59] L. Chen, F. Matsukura, and H. Ohno, Direct-current voltages in (Ga, Mn)As structures induced by ferromagnetic resonance, *Nat. Commun.* **4**, 2055 (2013).
- [60] M. Harder, Z. X. Cao, Y. S. Gui, X. L. Fan, and C. M. Hu, Analysis of the line shape of electrically detected ferromagnetic resonance, *Phys. Rev. B* **84**, 054423 (2011).
- [61] J. C. Sanchez, L. Vila, G. Desfonds, S. Gambarelli, J. P. Attane, J. M. De Teresa, C. Magen, and A. Fert, Spin-to-charge conversion using Rashba coupling at the interface between non-magnetic materials, *Nat. Commun.* **4**, 2944 (2013).
- [62] J. C. Rojas-Sánchez, M. Cubukcu, A. Jain, C. Vergnaud, C. Portemont, C. Ducruet, A. Barski, A. Marty, L. Vila, J. P. Attané, E. Augendre, G. Desfonds, S. Gambarelli, H. Jaffrès, J. M. George, and M. Jamet, Spin pumping and inverse spin Hall effect in germanium, *Phys. Rev. B* **88**, 064403 (2013).